Article

Prediction of electrode microstructure evolutions with physically constrained unsupervised image-to-image translation networks

Check for updates

Anna Sciazko ✉, Yosuke Komatsu, Takaaki Shimura & Naoki Shikazono

Microstructure of electrodes determines the performance of electrochemical devices such as fuel cells and batteries. The efficiency and economic feasibility of these technologies depend on the stability of the microstructures throughout their lifetime. Although modeling techniques were proposed for determining electrode performance from 2- or 3-dimensional microstructural data, it is still extremely challenging to predict long-term structural degradation by means of numerical simulations. One of the major challenges is to overcome the difficulties in obtaining experimental data of an identical sample through the degradation process. In this work, a machine learning-based framework for predicting microstructural evolutions with limited amount of un-paired training data is proposed. Physically-constrained unsupervised image-to-image translation (UNIT) network is incorporated to predict nickel oxide reduction process in solid oxide fuel cell anode. The proposed framework is firstly validated by simplified toy-problems. Secondly, the UNIT network is applied to real microstructures of solid oxide fuel cells, which results in excellent visual and statistical agreements between real and artificially reduced samples. The proposed network can predict evolutions in new microstructures, which have not been used during training. Furthermore, a conditional UNIT network (C-UNIT) was demonstrated, which can predict the microstructure evolutions based on process conditions as well as continuous time series of microstructural changes.

Solid oxide fuel cells (SOFCs) are characterized by high efficiency as well as fuel flexibility, but their drawback is the degradation due to high operating temperature in the range of 600–900 °C. The harsh operating conditions results in the microstructural evolution during operation. In particular, nickel (Ni) agglomeration and migration[1,2], Ni oxidation and reduction[3,4], ceramic support cracking[5,6], carbon deposition[7], phase segregation[8,9] and poisoning of impurities such as sulfur[10,11] are observed in the fuel electrodes. Several attempts have been undertaken to predict those changes at the microstructural level. Wang et al.[12] and Xiang et al.[13] attempted to model nickel depletion and coarsening with the phase field model. Jiao and Shikazono[14] proposed a method to simulate nickel oxide reduction process in the composite structure incorporating the volume change followed by the phase field simulation of particle sintering. Hara et at.[15] simulated Ni sintering with a Monte Carlo method. Even though successful results were obtained, such methods require a priori assumptions and simplifications in

the modeling, which cause difficulties in predicting complex and combined degradation phenomena.

The sizes of particles in SOFC electrodes are in the sub-micron range[11,16–20]. Recently, even finer microstructures with nano-particles are achieved by techniques such as infiltration and exsolution[5,21–23], etc. Typical observation techniques of SOFC electrode microstructures are scanning electron microscopy (SEM), transmission electron microscopy (TEM) and 3-D characterization by focused ion beam—scanning electron tomography (FIB-SEM)[24,25]. Measuring time-series changes of an identical sample using these techniques is challenging due to the destruction of the samples. Several samples from the same fabrication batch are usually observed, and their microstructural statistics are compared in the post-mortem characterization. Obtaining paired data of an identical sample before and after the processes is challenging, since it requires non-destructive imagining techniques. Nano-XCT is the only choice[26,27] to meet the resolution required for

Institute of Industrial Science, The University of Tokyo, Tokyo 153-8505, Japan. ✉e-mail: sciazko@iis.u-tokyo.ac.jp

1

the electrode microstructure analyses. In addition, several attempts were taken to observe the SOFC electrodes using operando techniques. Patterned electrodes under SOFC and SOEC operations were observed by a laser confocal scanning microscope by Komatsu et al. and Ouyang et al.[28,29]. Jeangros et al. developed measurement setup for a single-chamber SOFC operated inside an environmental TEM (E-TEM)[30]. However, those studies require simplifications in geometries and operation procedures.

Machine learning methods are widely used in processing and extracting information directly from large experimental datasets. The convolutional-based neural network (CNN) are well adjusted to process 2-D image and 3-D volume data[31–34]. However, they usually require high quality paired data for training. UNsupervised Image-to-image Translation (UNIT) network has become popular in many image processing applications such as style transfer, image colorization and object transfiguration[35], which can correlate two image domains without explicitly providing paired training examples. However, applications of UNIT to analyze electrode microstructures are scarce. A similar technique for unsupervised image translation, cycle-consistent generative adversarial network (CycleGAN) was successfully used for enhancing the quality of SEM images[36], correction of out-of-focus microscopic images[37] and transformation of the optical microscopy images[38].

Machine learning applications for fuel cells and porous materials have been rapidly evolving in recent years[39]. For SOFC applications, neural networks and fuzzy logic models were initially applied to optimize and predict SOFC performance[40]. Artificial neural networks (ANN) with a perceptron architecture with a limited number of input and outputs were incorporated for material screening[41], predictions of SOFC performance depending on operating conditions[42–44], flow field structure[45], electrode microstructural parameters[46], and SOFC stack electrochemical impedance spectra (EIS)[47]. Moreover, coupling ANN with algorithms such as swarm optimization[46,48] and genetic algorithm[45,46,49,50] provided new strategy for system optimization. Recently, more complex neural networks are applied for processing time series data and for analyzing SOFC microstructures. Recurrent neural networks (RNN) and long-short time memory networks (LSTM) utilize sequential information as the input data, which were applied for SOFC fault diagnosis[51], prediction of remaining lifetime[52] and prediction of EIS and DRT degradations[53]. Applications of convolutional neural networks (CNN) and generative adversarial networks (GAN) for SOFC and porous materials microstructures, e.g. image segmentation, super-resolution, parameter prediction and artificial structures generation, have been receiving great attention. The semantic segmentation algorithms based on various CNN architectures were proposed for identifying the phases in raw SEM and FIB-SEM images[54–56]. Super resolution CNN based algorithm was proposed to improve the resolution of optical microscope images to SEM-alike quality[57]. Sequential FIB-SEM images were super-resolved in the stacking direction[58]. Furthermore, CNNs have been used in material engineering to extract microstructural properties such as effective diffusivity[34,59], ionic conductivity[60], elastic deformations[61], and electron back-scatter diffraction patterns[62], etc. The CNNs successfully predicted parameters of anodes[63] and cathodes[64] from their microstructures. The generative machine learning was utilized for fabricating artificial SOFC microstructures. Gayon-Lombardo et al.[33] and Hsu et al.[65] demonstrated successful applications of GANs to synthesize 3-D SOFC microstructures. Kishimoto et al.[66] synthesized microstructures with predefined properties by conditional GAN, and Sciazko et al.[31] reconstructed 3D microstructures from 2D cross-sectional images by GAN. Machine learning was also successfully utilized for detecting materials degradation and failure occurrence[67]. However, applications of machine learning tools to predict microstructural changes of electrodes are still limited.

In this work, a framework to predict microstructural changes by the physically constrained UNIT network is proposed. The validity of the proposed approach is tested for the NiO reduction process in the Ni-based SOFC fuel electrodes. The volume of NiO decreases by 41% during the reduction process[68], and the reduced Ni 3D microstructures depend on the reduction conditions such as temperature[69,70] and gas composition[69,71]. Moreover, the

effects from the interactions between supporting ceramic material and NiO particles cannot be excluded[72,73]. The reduction process greatly influences the electrode morphological parameters such as triple phase boundary density (TPB), Ni network connectivity and pore tortuosity, which determines electrode's electrochemical performance. In addition, it was reported that initial electrode microstructure after the reduction process influences long term degradation[70]. Understanding the reduction mechanism is highly relevant for predicting electrode degradation during reduction/oxidation (redox) cycles occurring under fuel-rich and fuel-lean cycling conditions[73,74].

Here, microstructure degradation due to the NiO reduction process is treated as the computer vision problem for the image-to-image translation. As the paired training images of an identical sample before and after the NiO reduction are very difficult to obtain, it is necessary to apply unsupervised training approach. In the unsupervised training, only available information is two independent sets of image data in which one consists of images in an arbitrary domain and the other consists of images in another domain. However, the paired examples demonstrating dependance between images in both domains do not exist. In the present study, we propose a method using UNIT with an additional physical constraint incorporated into the UNIT generator loss function enforcing the partly known physical phenomena. The network is trained with un-paired SEM images from the nickel oxide (NiO)-yttria stabilized zirconia (YSZ) and NiO-gadolinium doped ceria (GDC) electrodes. In addition, conditional UNIT (C-UNIT) is trained to capture the influence of reduction temperature as well as predicting the microstructure dependance on reduction time.

Results and discussion
Validation

The validity of the present method was confirmed with the toy-problem tests equivalent to the simplified reduction process as shown in Figs. 1–3. Three types of toy-problems were carried out for the following purposes: (I) determining interdomain translation operator for predicting structural changes in the same class of microstructures, (II) predicting evolution in new microstructures and (III) extrapolating the prediction for the new process depending on the external conditions. Two data domains were defined, where domain A consists of spherical particles with a diameter of 15-pixels (pointed by green color) and 4-pixels core (red color). Domain B consists of analogical 8-pixels diameter particles with 4-pixels core. The red core particle is assumed to be immobile during the translation process, and this constraint is introduced in the generator loss function. Training data for the UNIT network have been prepared by randomly placing the particles in space independently for both Domains A and B. While the statistical characteristics of the particles in both domains are known, an image translation operator between the domains is not available, as there are no explicit examples demonstrating how images from Domain A are translated into Domain B.

In the first toy problem, a single particle was placed in each domain (Fig. 1a). The UNIT network can discover the translation pattern directly from the unpaired training data. The network outputs a particle with identical spatial position but different diameter of the green particle (Fig. 1b). The comparison between UNIT predictions and ground truth data for 200 samples gives the pixel-wise accuracy of over 99.6%. In the next validation attempt, 10 particles are randomly placed in each domain allowing overlaps. The UNIT reproduces this complicated translation with an accuracy over 98% (Fig. 1c, d).

The ability of the UNIT to predict changes in new microstructures which were not used in the training dataset was tested in the second toy problem. Samples with various porosities controlled by the numbers of particles were used for training. The training data were samples with 11–20 and 191–200 randomly placed particles, representing high and low porosity structures, respectively. Testing was conducted for the samples with full spectra of porosities, i.e. 1–200 particles randomly placed in the domain. The original size of the prepared data was 256 × 256 pixels, while the training was conducted with the randomly extracted patches of 64 × 64 pixels as shown in Fig. 2a. Prediction of the trained UNIT network are shown in Fig. 2b. The UNIT provides excellent prediction not only for the low and high porosity
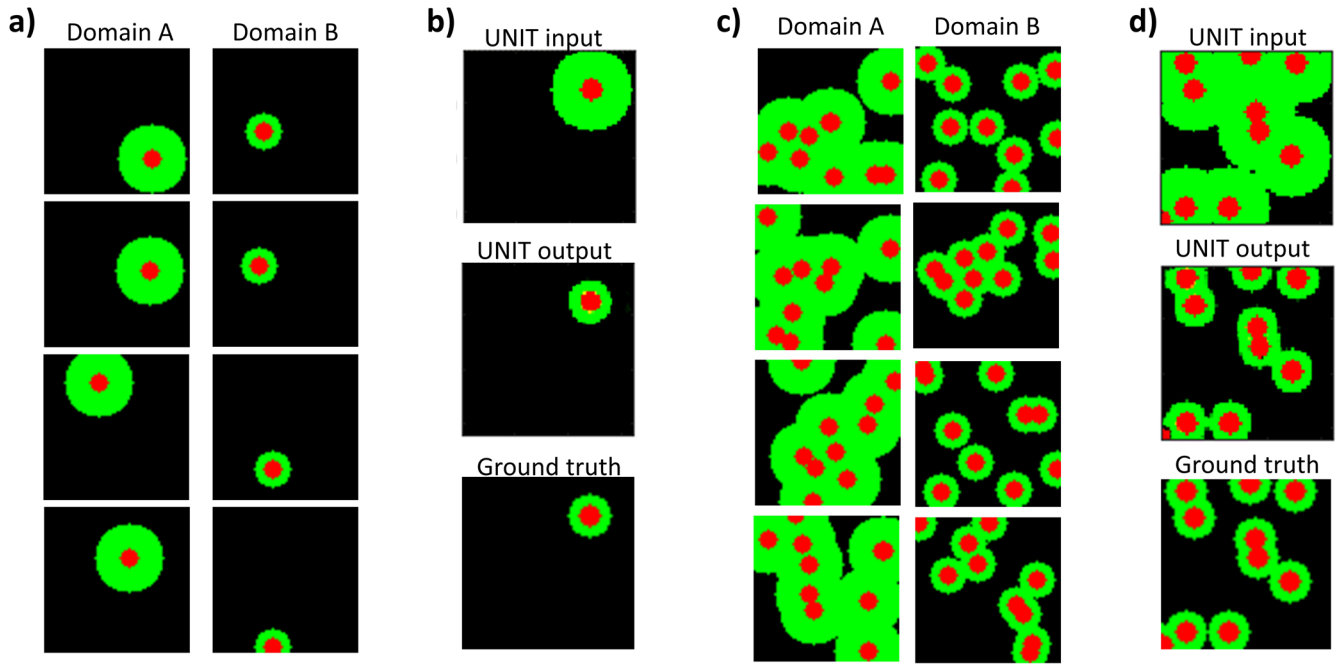
Fig. 1 | Validation toy problems with single and multiple particles. a, **c** Training data; **b**, **d** input and output of UNIT and ground truth.
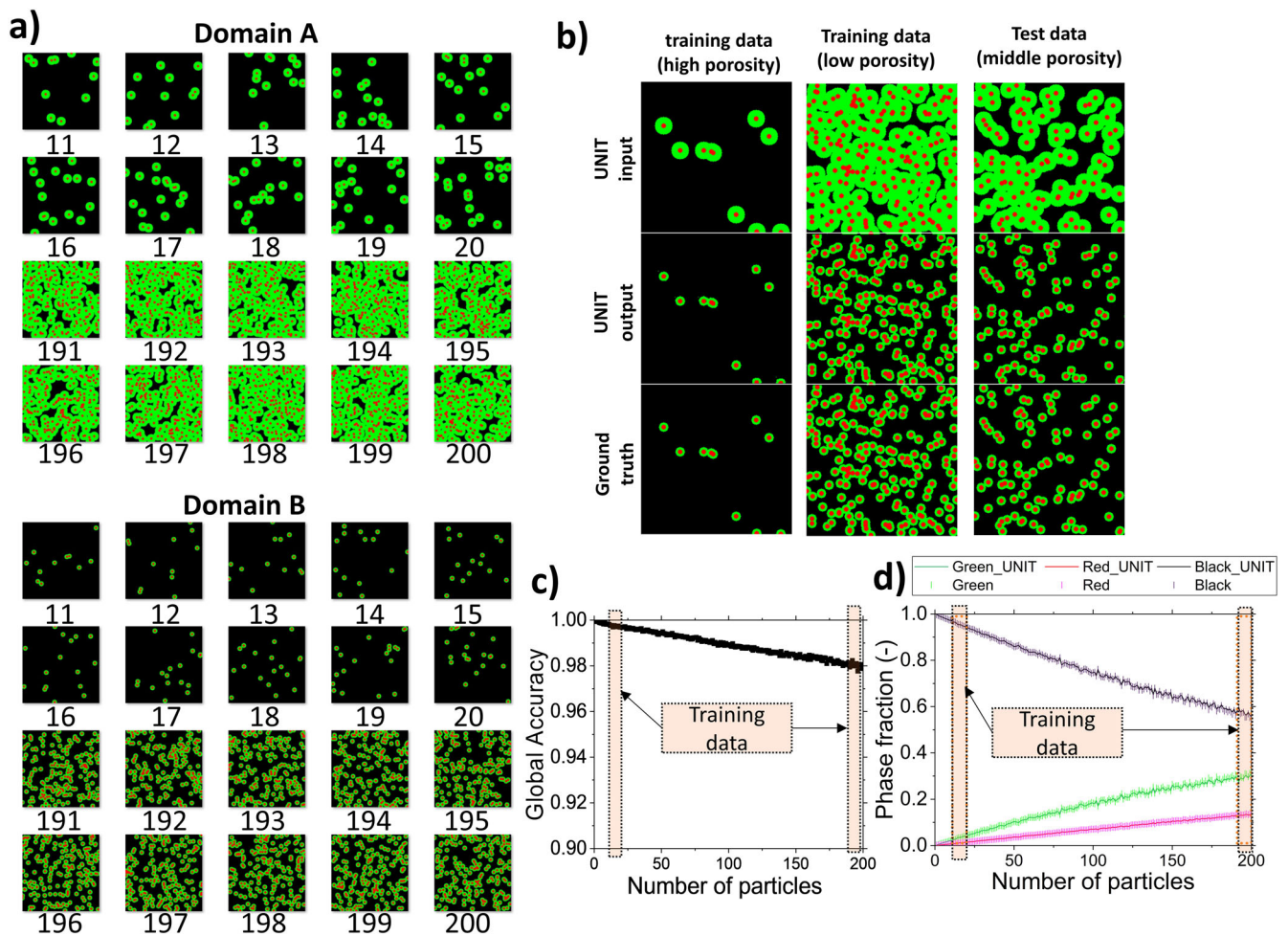

Fig. 2 | Validation toy problem for samples with various porosities. a Training data (11–20 and 191–200 particles in the domain), **b** input and output of UNIT and ground truth for samples with high, low and middle porosities, **c** global pixel-wise accuracy and **d** predicted phase fractions.
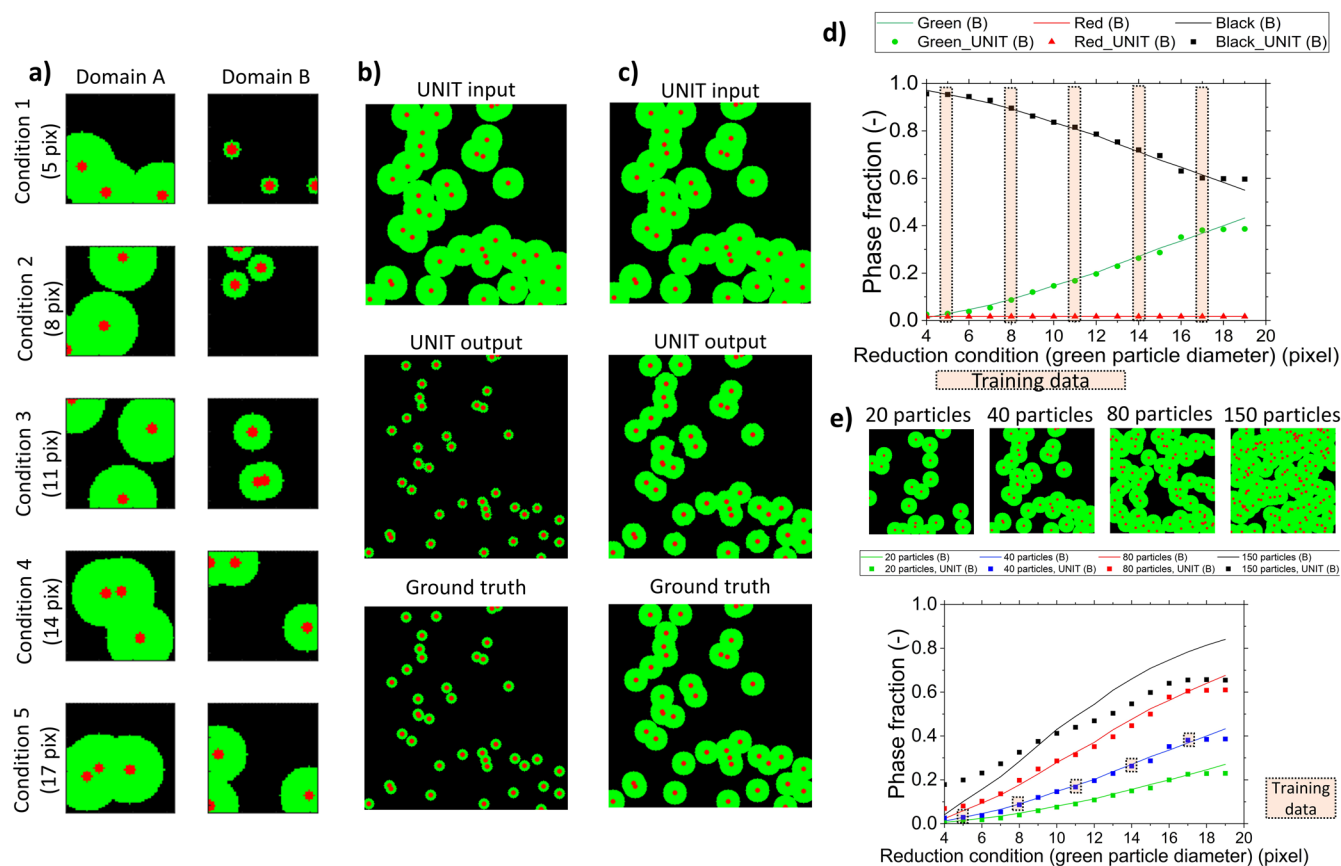
Fig. 3 | Validation toy problem depending on external condition. a Training data with conditional output. Input and output of C-UNIT and ground truth for conditions of **b** 7 and **c** 15 pixels. **d** Predicted phase fractions. **e** Microstructures with various porosities and predicted phase fractions.

structures, but it works well for all samples with pixel-wise accuracy over 98% (Fig. 2c). From Fig. 2d, it is seen that phase fractions are almost ideally reproduced.

The third validation toy problem starts with an assumption that the simplified reduction process depends on the external condition which determines the diameter of the green particles in Domain B. The diameter of the green particles in Domain A was always kept as 20 pixels, while the diameter of particles in Domain B was varied between 4 – 19 pixels. This can be understood as the dependence of microstructure on hydrogen exposure time. The UNIT network was modified, in which additional information of the condition was included as the input to both generator and discriminators. Examples for five different conditions, i.e. green particle diameters of 5, 8, 11, 14 and 17 pixels, were used for network training as shown in Fig. 3a. The prediction results for the trained C-UNIT network are shown in Fig. 3b, c for the new conditions not used in the training process. As shown in Fig. 3d, C-UNIT can predict well the dependance not only for data from the training dataset, but it also successfully predicts for the new conditions. In addition, as shown in Fig. 3e, the generalization capability of the C-UNIT network was tested for four different microstructures with various porosities. The test samples with 20, 40, 80 and 150 particles in Domain A have porosities of 70, 54, 29 and 14%, respectively. Global pixel-wise accuracy over 95% is achieved for samples with high to middle porosity structures. The C-UNIT prediction for the sample with initial porosity of 14% has discrepancies compared with the grand truth structure even though the overall pixel-wise accuracy is over 85%. This is due to the significant structural difference from the training data, in which the network was trained with samples with porosity of approximately 50%. The particles highly overlap with each other in the dense samples, and this type of training examples have not been provided during the training. In order to improve the results for dense microstructures, it is desired to provide similar examples for network training. In addition, the prediction accuracy of large green particles with diameter of 19 pixels is slightly lower

than other conditions. The training data contained particles only up to 17 pixels. Thus, the 19 pixel particles are beyond the training range. As illustrated by these facts, extrapolation using a neural network trained on a specific data range can potentially lead to errors.

Microstructure change during NiO-YSZ reduction

Firstly, the UNIT network was applied to predict NiO reduction process at 800 °C. The real as-sintered NiO-YSZ and as-reduced Ni-YSZ microstructures are shown in Fig. 4a. The microstructures were taken from two different samples in the same fabrication batch. Artificially reduced Ni-YSZ structure is the output of the trained UNIT network. Prediction is conducted for the same NiO-YSZ input data, as it was used for training UNIT. Even though the training was conducted with smaller data patches, the UNIT network can predict changes in the new microstructure of any size. The YSZ phase is not changed as it is assumed that YSZ backbone is immobile during the reduction process. The theoretical composition in Fig. 4b is calculated from the theoretical volume change of NiO into Ni assuming full reduction of NiO using the as-sintered sample before reduction. Good agreement is observed between the volume fractions of real and artificially reduced samples. Increase in porosity represents the phase change from NiO to Ni. The UNIT reduced Ni-YSZ has not only a good visual agreement with real Ni-YSZ, but also shows good agreement in statistical characteristics as shown in Fig. 4b–e. UNIT can reproduce well the volume fractions, surface and TPB densities, which are crucial for electrochemical performance.

Additional validation is carried out with new NiO-YSZ microstructure images that were not part of the UNIT training dataset, as shown in Fig. 5. The predictions with new data are comparable to the prediction with training images in terms of both visual and statistical parameter accuracy. The slight difference in the YSZ surface area of artificially reduced sample S2 is due to the quality of the original input data. The TPB density is slightly underestimated by approximately 6%.
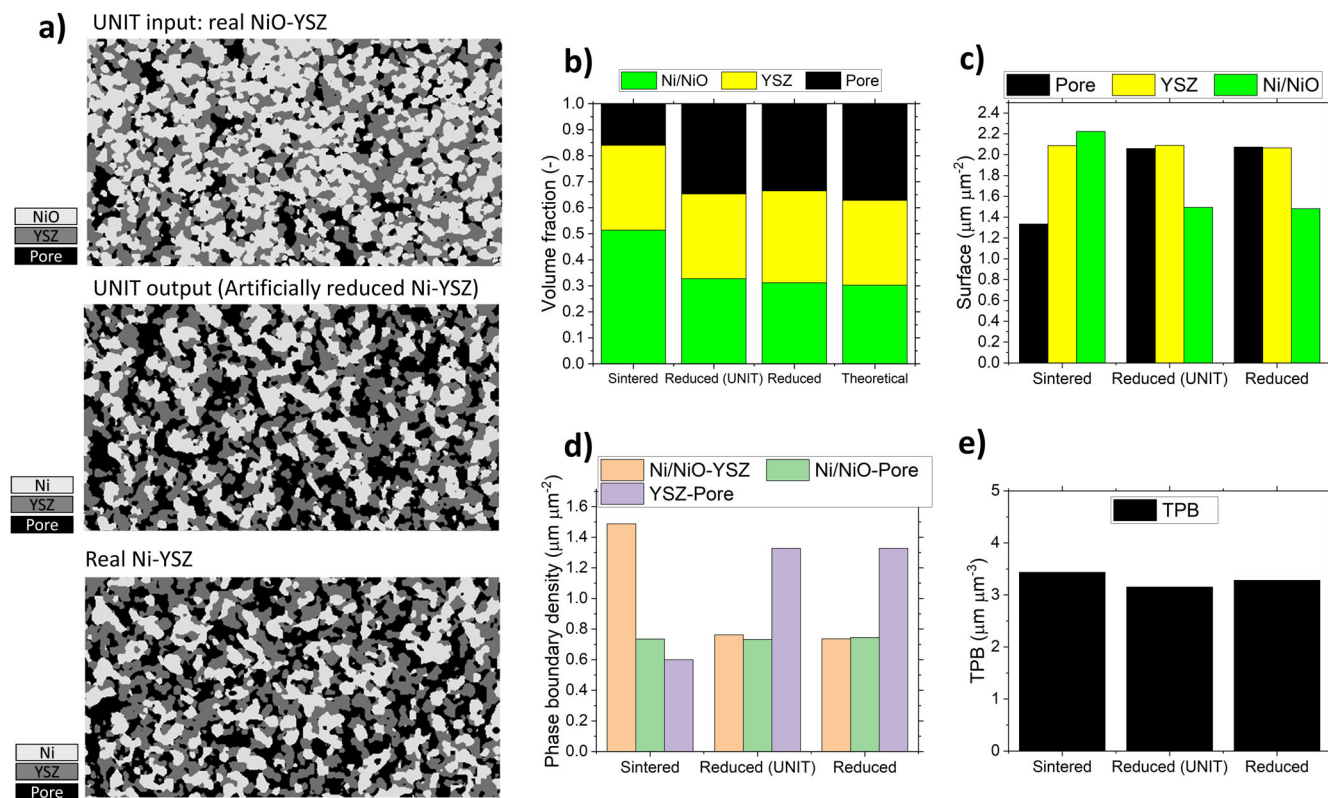
Fig. 4 | Prediction of microstructure change during NiO-YSZ reduction. a Real NiO-YSZ, artificially reduced Ni-YSZ and real Ni-YSZ microstructures (real data are taken from the training dataset). Comparison between sintered, real reduced and artificially reduced (UNIT) microstructures: **b** volume fraction, **c** surface area density, **d** phase boundary density, and **e** TPB density.

Prediction of new microstructures

In this subsection, UNIT network was trained using samples Ni50GDC50 (Ni : GDC = 50: 50 vol%) and Ni60GDC40-IP (Ni: GDC = 60: 40 vol% with low porosity), where IP denotes a sample made by isostatic pressing. These samples have different Ni and pore volume fractions as shown in Fig. 6a. Volume fraction and surface area density were selected as the representative microstructural parameters for the evaluation. The trained UNIT can predict microstructural change during reduction very well for samples used in the training dataset. Moreover, it can also generate microstructures with new properties as shown for the Ni60GDC40 sample which is not used for training. This implies that the network can be trained with limited number of real experimental data, and can be utilized for predicting variable parameters.

Reduction at various temperatures

It is well known that the reduction temperature strongly influences the microstructures of Ni-based composites. Reduction of bulk NiO crystals by hydrogen has been studied at different temperatures in the range of 270 and 1320 °C[75], where complex porous network appeared at reduction temperature below 900 °C. In the present study, NiO-YSZ was reduced at 500, 600, 800 and 1000 °C as shown in Fig. 7a, which follows the abovementioned behavior. Although the volume fractions of all samples after reduction are very close to the theoretical, the microstructures strongly depend on the reduction temperature. The samples reduced at lower temperature are characterized by large number of small pores inside the Ni particles, while higher reduction temperature results in larger pores.

The C-UNIT network was trained with Ni-YSZ samples reduced at various temperatures as shown in Fig. 7b. As can be seen in Fig. 7c, d, C-UNIT can predict well the dependence of microstructure on temperature, not only for the temperatures used for training, but also for temperatures which were not used for training. The prediction accuracies are similar for the data in both the training dataset and the testing set. However, there is a difference in the shape of the nano-pores between real and artificially

reduced samples at 500 °C. This may be due to the structure of the UNIT network, which relies solely on convolutional layers. In general, U-net configuration is superior to the encoder-decoder architectures in preserving small image details. Modifying the structures of UNIT network with skipped connections may also help to overcome this issue. In addition, the discrepancy may be due to the variation of YSZ phase fraction between different samples in the training data, which might be caused by the size of training image or by the accuracy of segmentation.

Predictions for temperatures in the range of 400–1100 °C are shown in the Supplementary Video 1. It is clear that the reduction initially progresses within the NiO grains by forming complicated inner pore network. The changes in shape and size from the original NiO grains are minimal. At higher temperature, the inner pores disappear and Ni particles coarsen, resulting in increased size of pores. The different final structures are the result of competition between chemical reaction and Ni sintering, which are both enhanced at higher reduction temperature.

Time-dependent reduction process

Shimura et al. [73] observed dynamic changes of Ni-YSZ microstructures during oxidation and reduction. The samples were reduced at 800 °C in pure H₂, and the microstructures are observed at different times. The pore structure formation inside the reduced Ni was observed in the initial period. The reduction is almost completed within 30 s of exposure to H₂ gas. After the reduction reaction, sintering of Ni phase progresses and the pores inside Ni disappears.

Here, an attempt is taken to model the time dependent reduction process by the C-GAN network. NiO-YSZ samples were reduced for 5, 15, 30 and 3600 s, as shown in Fig. 8a. The pores inside NiO grains in the initial NiO-YSZ structure are due to the redox treatment prior to the reduction test. The details of experimentation can be found in our previous work[73]. Ni and NiO phases are not distinguished in this study, as it was not possible to identify them from the collected SEM images
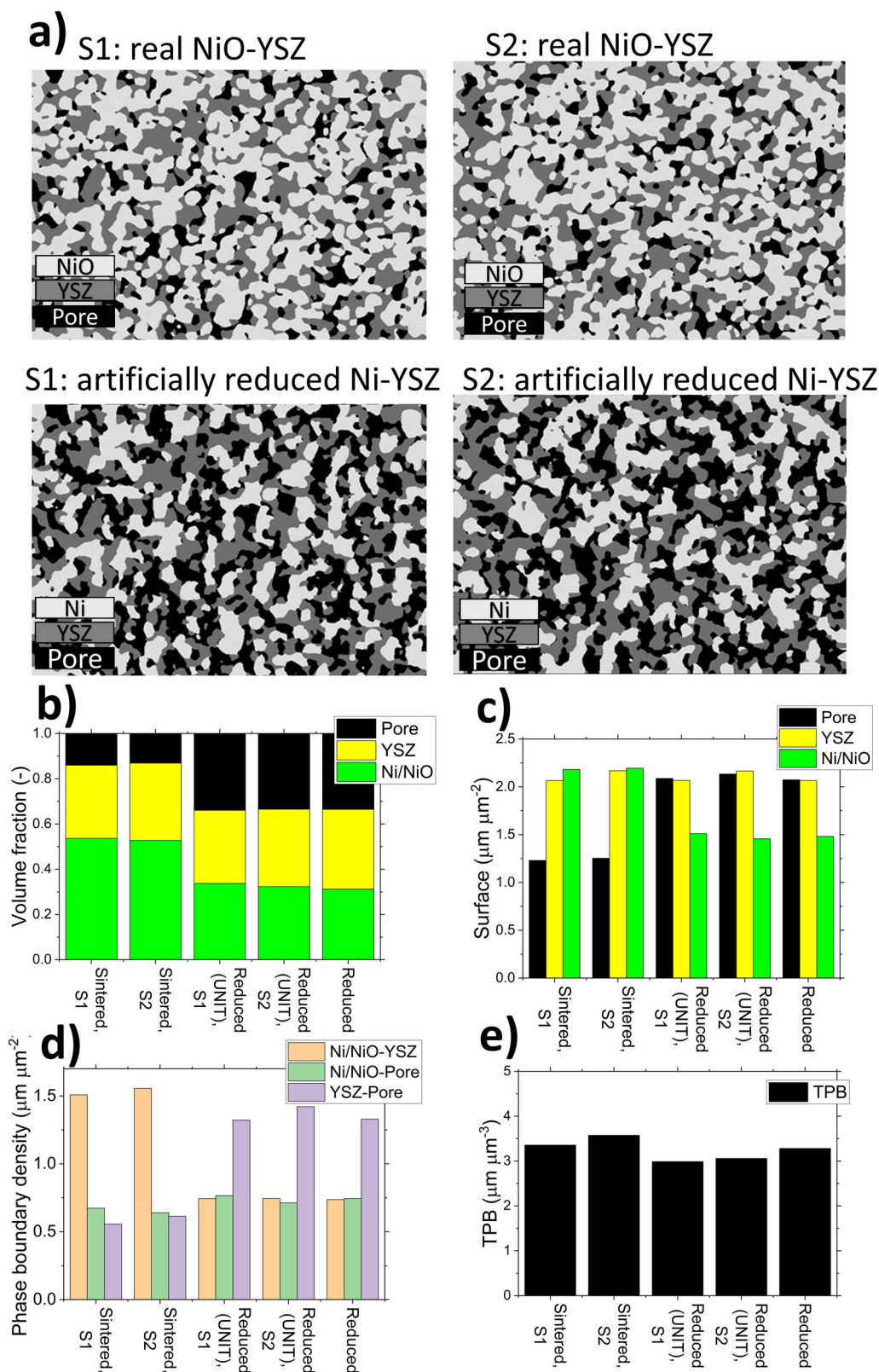
Fig. 5 | Validation with new NiO-YSZ microstructures. a Artificially reduced Ni-YSZ from real NiO-YSZ samples S1 and S2. Comparison between sintered, real reduced and artificially reduced (UNIT) microstructures: **b** volume fraction, **c** surface area density, **d** phase boundary density, and **e** TPB density.

Two independent C-UNIT networks, i.e. C-UNIT$_{reduction}$ and C-UNIT$_{sintering}$, were trained to predict initial reduction and following Ni sintering processes. Two data points, 30 and 3600 s, were used for C-UNIT$_{sintering}$, and microstructures at 0, 5, 15 and 30 s were used to train C-UNIT$_{reduction}$. The conditional UNIT architecture was chosen for

C-UNIT$_{sintering}$ instead of conventional UNIT to simulate intermediate time points, even though only two training data are available. The details of the training data in each domain are given in Fig. 8b.

The results of combined C-UNIT$_{sintering}$ and C-UNIT$_{reduction}$ networks are shown in Fig. 9 and in the Supplementary Video 2. As the
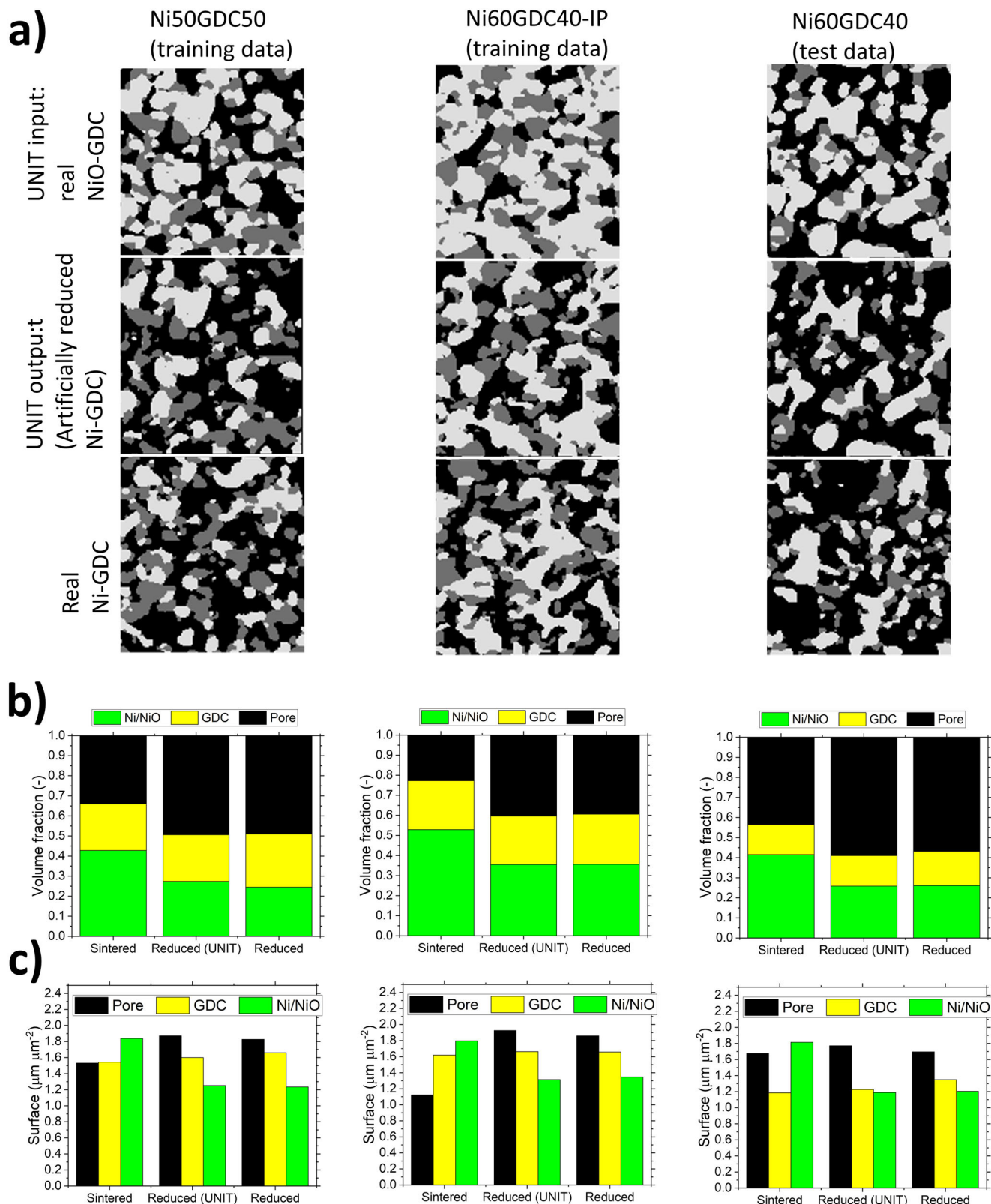
Fig. 6 | Prediction of NiO reduction in NiO-GDC microstructures with varied properties. a Real NiO-GDC, artificially reduced Ni-GDC and real Ni-GDC microstructures with various compositions. Comparison between sintered, real reduced and artificially reduced (UNIT) microstructures: **b** volume fraction and **c** surface area density.
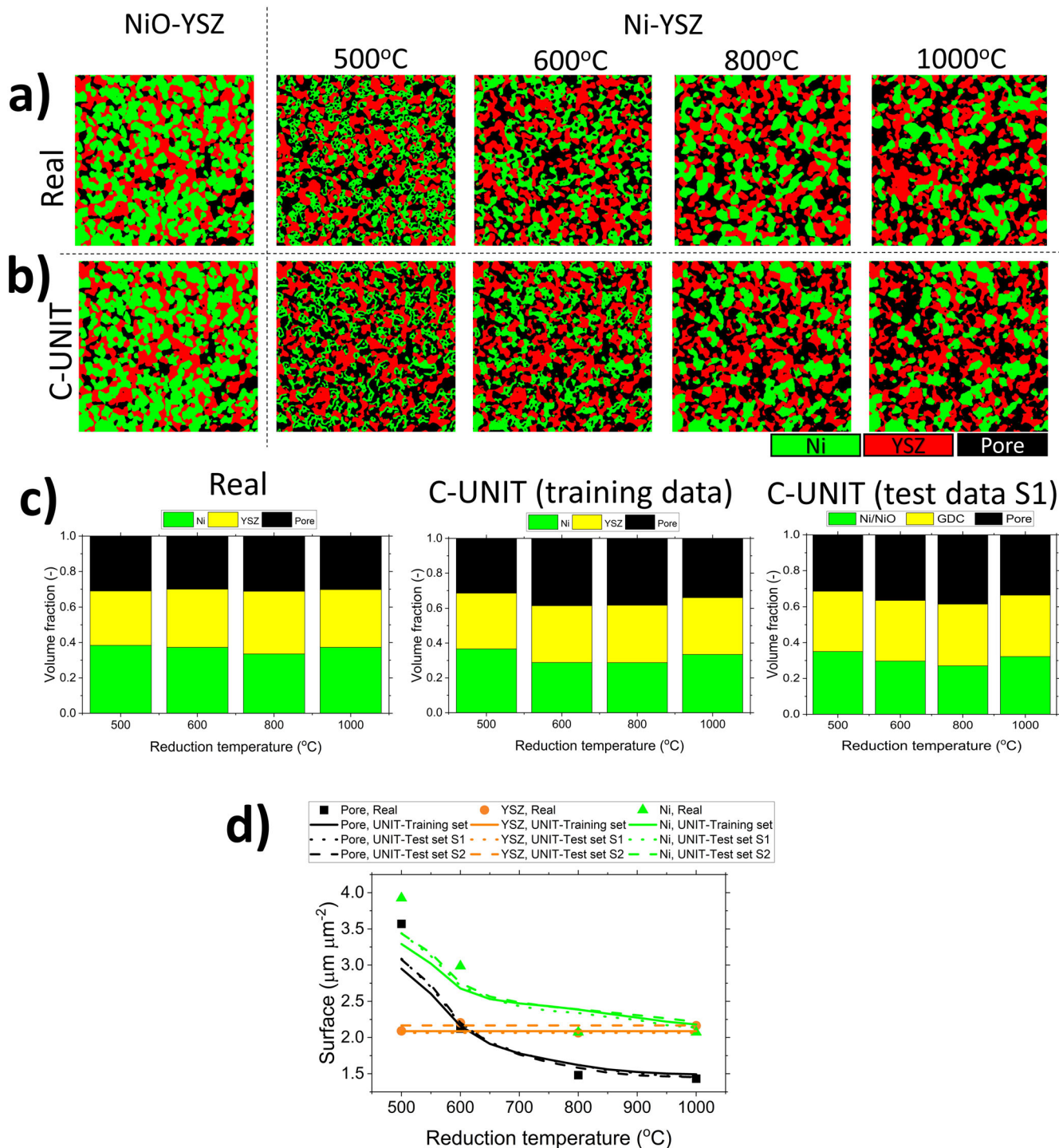
Fig. 7 | NiO-YSZ samples reduced at various temperatures. a Real and **b** artificial microstructures, **c** volume fractions and **d** surface area density.

generalization ability of UNIT network was already demonstrated in previous subsections, only the prediction with training data is shown. The predicted volumes fractions and surface areas are in reasonable agreement with the real structures. The error in the predicted values is shown in Supplementary Fig. 1. The largest error is observed in the predictions of pore and YSZ, which falls within the range of 10%. This resulted from the errors in the initial phase segmentation of training data. NiO grains have large inner pores, which are difficult to segment as resin could not be infiltrated during FIB-SEM measurement. Moreover, the variation between the samples for training is quite large, i.e. YSZ fraction varies significantly in the training data which should be the same for all the samples. As YSZ

immobility constraint is imposed, this variation is compensated by the shapes of other phases. Decrease of NiO and increase of pore represent the reduction process. The most significant volume change occurs during initial 5 s of the reduction process, i.e. the size of NiO particles decreases from the circumference and the size of the original large pores increase. At the same time, inner pores appear inside the NiO particles. From 5 to 30 s, reduction progresses and the size and number of inner pores increase. The size of large pores does not change, which implies that the reduction process proceeds mostly at the core of NiO particles. This is consistent with the complex inner pore structures reported in the literature. Reduction of NiO is followed by sintering of Ni, which is well reproduced by the C-UNIT. Large Ni particles
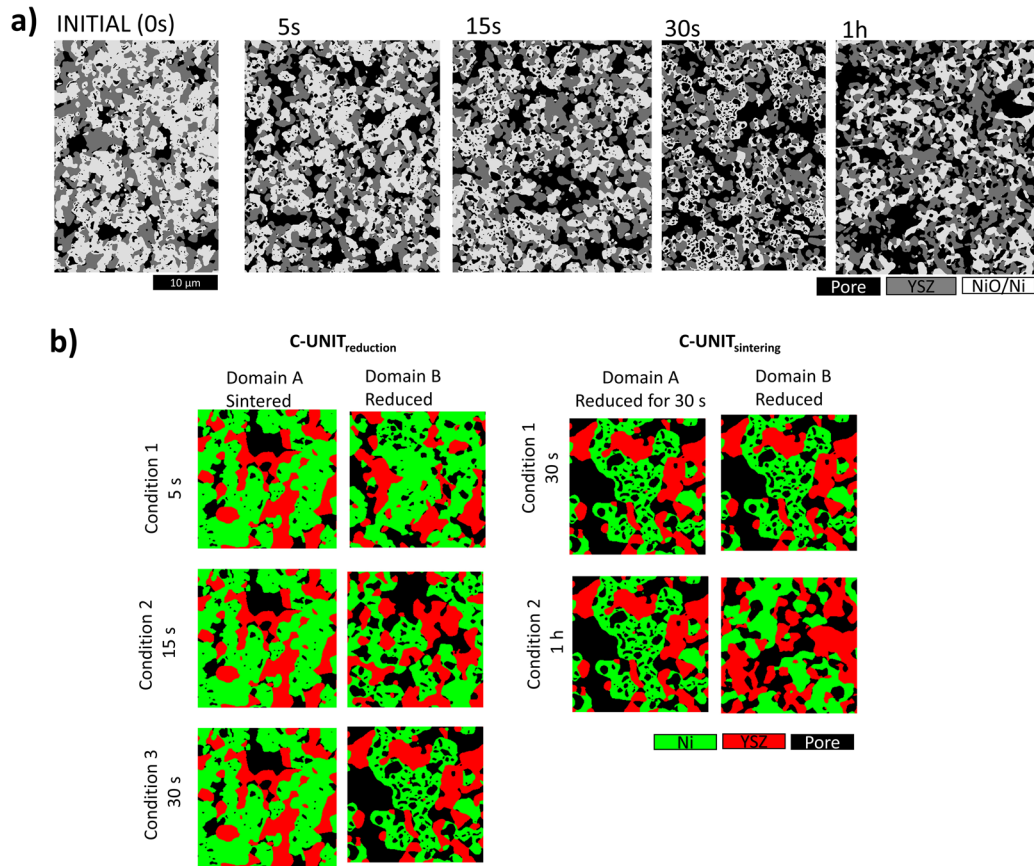
Fig. 8 | Reduced NiO-YSZ samples at various times. a Segmented SEM images and **b** training data for C-UNIT$_{sintering}$ and C-UNIT$_{reduction}$ networks.
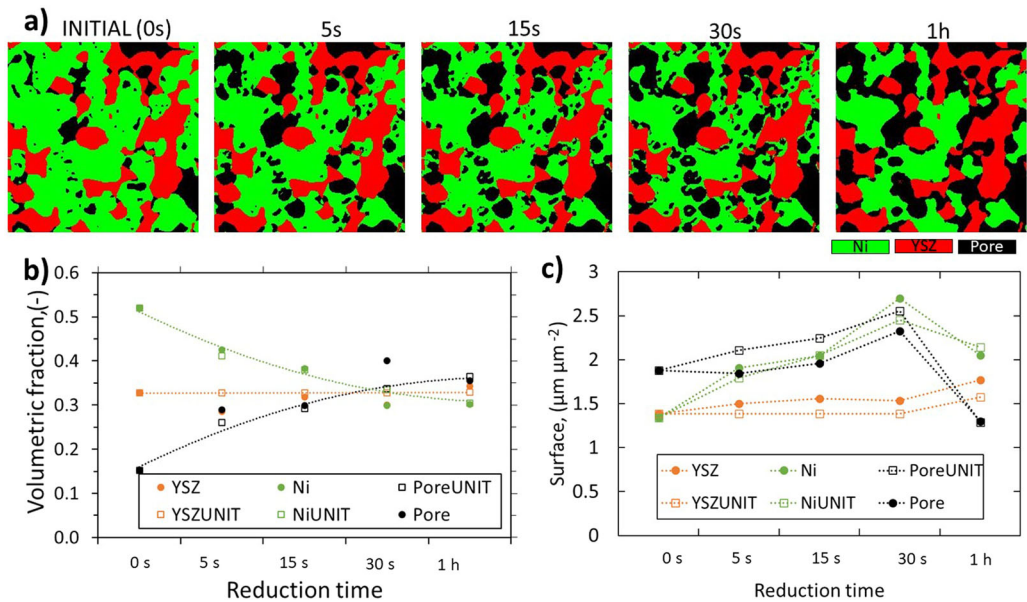

Fig. 9 | Results of training network for time-dependent prediction. a NiO-YSZ reduced structures predicted by C-UNIT$_{sintering}$ and C-UNIT$_{reduction}$, comparisons of **b** volume fraction and **c** surface area density.

grow on the expense of small Ni structures. In addition, the C-UNIT network can predict stable Ni-YSZ interfaces.

Future perspectives
A framework for predicting microstructure changes in SOFC electrodes using a conditional unsupervised image-to-image translation network with physical constraints is proposed. UNIT and C-UNIT networks were used to predict the reduction process of Ni-based SOFC electrodes from unpaired training data. The networks were trained with image patches of NiO-YSZ and Ni-YSZ microstructures before and after reduction. A physical constraint was included in the generator loss function to constrain YSZ and GDC backbones, which are assumed to be immobile during the reduction process.
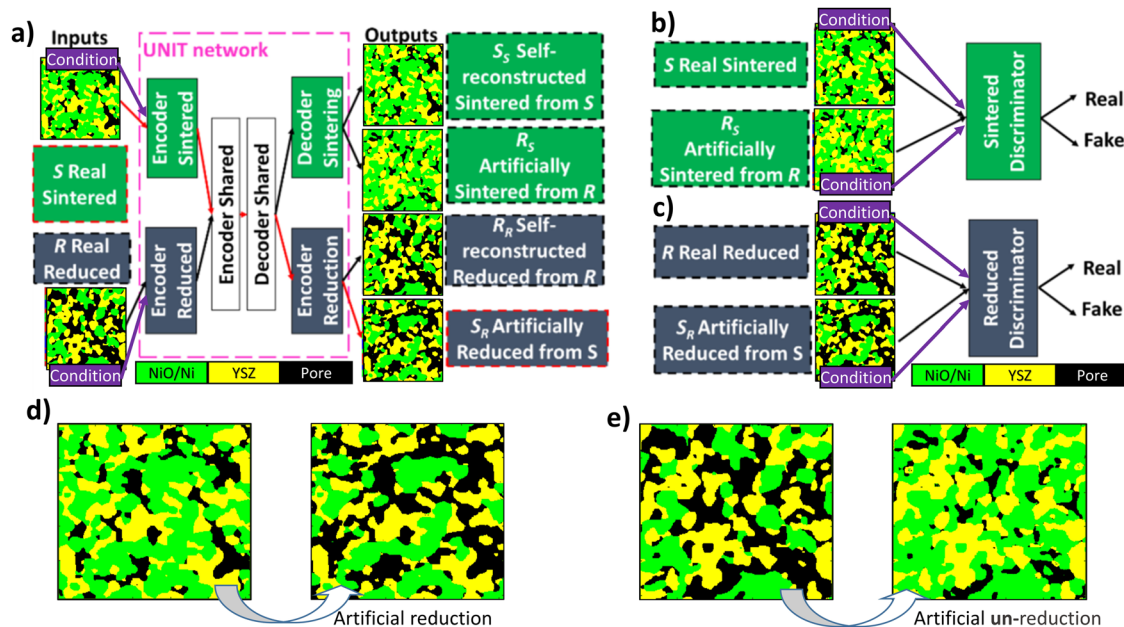
Fig. 10 | Structure of UNIT network. a UNIT generator network, **b** sintering discriminator and **c** reducing discriminator. Image patches processed by UNIT for **d** artificial reduction and **e** artificial un-reduction (the YSZ phase is assumed to be immobile).

The reduced microstructures predicted by the UNIT show excellent visual and quantitative agreements with the real samples. Furthermore, UNIT can predict microstructural changes in samples that were not used for training.

C-UNIT which is conditioned by temperature can predict the microstructure changes at various reduction temperatures. In addition, the C-UNIT can predict time-dependent microstructure evolution process. The proposed method has a potential to predict various microstructure evolution processes not only NiO reduction, but also many processes which are important for degradation studies.

This study investigated the applicability of physically constrained UNIT and C-UNIT in 2D problems. However, in order to fully understand the SOFC degradation processes related to their microstructural changes, it is necessary to analyze 3D data. The future work will focus on the extension of the present 2D UNIT to 3D space. This will provide more accurate analysis and potential for precise 3D electrochemical calculations. However, there are significant challenges associated with the extension to 3D, primarily related to data collection and network training. Measuring 3D data requires more complex experimental techniques such as FIB-SEM, which takes 12 to 36 hours to measure a single microstructure. This problem can be potentially solved by applying machine learning to generate artificial 3D models from 2D cross-sectional images[31]. In addition, it is anticipated that the proposed data patching and augmentation techniques will be helpful in reducing the amount and volume of the raw sample set required. Another challenge which must be considered is the considerable time and memory resources required for the training the 3D UNIT network.

This study aims to demonstrate the usability of UNIT and C-UNIT to predict complex shape change phenomena in porous microstructures. Further improvements of the network structures, e.g. hyperparameters and learning strategy are necessary. Moreover, extension of the methodology may include combination with the LSTM networks. Additionally, UNIT and C-UNIT networks can be very useful for generating training data for physics informed neural networks (PINN) which requires paired data[76]. Utilizing PINN networks for the inverse problems can identify the physical parameters describing degradation processes.

We demonstrated that UNIT and C-UNIT can successfully predict NiO reduction process. It is expected that this technique can be further utilized for other microstructural changes, e.g. Ni migration during SOEC operation, Ni coarsening under high current density and humidity, carbon deposition, segregation of impurities, ceramic support cracking, etc. Moreover, present approach can be applied to other porous multiphase materials such as polymer electrolyte fuel cells, batteries, photovoltaic cells, catalytic reactors and membranes, etc.

Methods
Physically constrained UNIT network
A schematic illustration of the UNIT network is presented in Fig. 10. The UNIT network is a type of generative adversarial neural network which consists of single generator and two discriminators. Two images represent source and target domains, i.e. NiO-YSZ (x_1) and Ni-YSZ (x_2) microstructures, are used as the UNIT generator input. The UNIT network generates four output images, among which two are source-to-target ($x_1^{1\rightarrow2}$) and target-to-source ($x_2^{2\rightarrow1}$) translated images. In this context, the source-to-target translation represents an artificial reduction from NiO-YSZ to Ni-YSZ (Fig. 10d), and the target-to-source translation can be understood as the artificial "un-reduction" of Ni-YSZ to NiO-YSZ. The "un-reduction" is not

Table 1 | Generator architecture

Number of downsampling blocks	2
Number of residual blocks in encoder and decoder subnetworks	5
Number of shared residual blocks in encode and decoder subnetworks	2
Number of filters in first convolution layer	64
Filter size in first and last convolution layers	7
Filter size in intermediate convolution layers	3
Padding	Mirrored values of the input, excluding the edge values
Weight initialization used in convolution layers	He Initialization
Activation function	Rectified Linear Unit
Activation function after final convolution	Hyperbolic tangent
Input size	64 × 64 × 3 or 256 × 256 × 3
Output size	64 × 64 × 3 or 256 × 256 × 3

the oxidation process, but rather can be understood as the inverse translation operator, which shows how the sample used to look like before reduction. The other two UNIT generator outputs are self-reconstructed images, i.e. source-to-source ($x_1^{1\to1}$) and target-to-target ($x_1^{2\to2}$) translated images. The generator network consists of three subnetworks in both encoding and generative parts to follow variational autoencoder (VAE) architecture. An additional input condition C, representing the reduction temperature or reduction time, is included as the input for C-UNIT network. The specifications of the generator and discriminator network architectures are given in Tables 1, 2, respectively.

The multifactor loss function is incorporated to jointly solve learning problems of VAE and GAN for image reconstruction, translation and cycle-reconstruction streams, as well as to fulfill physical constraint. Generator loss function L_{gen} is calculated as:

$$L_{gen} = w_1 \bullet L_{self} + w_2 \bullet L_{cycle} + w_3 \bullet L_{KL} + w_4 \bullet L_{KLcycle} + w_5 \bullet L_{adv} + w_6 \bullet L_{physic}, \tag{1}$$

where individual losses are defined as:

$$\text{self} - \text{reconstruction loss}: L_{self} = ||X_{real} - X_{self-reconstructed}||_1, \tag{2}$$

$$\text{cycle consistency loss}: L_{cycle} = ||X_{real} - X_{cycle-reconstructed}||_1, \tag{3}$$

$$\text{hidden KL loss}: L_{KL} = \left(X_{esa|self-reconstructed}\right)^2, \tag{4}$$

$$\text{cycle hidden KL loss}: L_{KLcycle} = \left(X_{esa|cycle-reconstructed}\right)^2, \tag{5}$$

$$\text{and adversarial loss}: L_{adv} = \left(1 - \bar{X}_{trans}\right)^2. \tag{6}$$

Additional physics loss L_{physic} is included in the generator loss to enforce the physical constraint, which is the immobility of ceramic backbone during the reduction process:

$$L_{physic} = ||X_{real|YSZ} - X_{trans|YSZ}||_1, \tag{7}$$

where $||\bullet||_1$ represent the L1 distance between the input images and the translated images. X_{real}, $X_{self-reconstructed}$ and $X_{cycle-reconstructed}$ are real, self-reconstructed and cycle reconstructed images, respectively. $X_{esa|self-reconstructed}$ and $X_{esa|cycle-reconstructed}$ are activations of the encoder shared block in the self-reconstruction and cycle reconstruction streams, respectively. $\bar{X}_{trans}$ represents the predictions of the discriminator on generated images. $X_{real|YSZ}$ and $X_{trans|YSZ}$ represent the YSZ phase in the real and respective translated images.

The discriminators' loss function L_{dis} are defined as:

$$L_{dis} = \left(1 - \bar{X}_{real}\right)^2 + \left(0 - \bar{X}_{trans}\right)^2, \tag{8}$$

where $\bar{X}_{real}$ and $\bar{X}_{trans}$ are the predictions of the discriminator on real and generated images, respectively. The discriminator loss function is calculated separately for as-sintered (NiO-YSZ) and as-reduced images (Ni-YSZ).

During the training step, patches of real microstructures are randomly extracted from full-sized SEM image to increase the training dataset. In addition, geometrical augmentation is applied by random rotation and flipping of the images as shown in Supplementary Fig. 2. The training is conducted with the phase-segmented images and the network uses "one-hot" encoding method proposed by Gayon-Lombardo et al.[33]. The image patches have 64×64 and 256×256 pixels for toy validation and real microstructures, respectively. The numbers of incorporated training images and their size are shown for each of the analyzed cases in Tables 3, 4 for toy-problems and real NiO-based electrodes, respectively. For the toy problems, training and validation data were prepared by randomly placing the particles in the domain. The particles were independently placed at different positions for oxidized and reduced domains for the training data. On the other hand, for the validation data, the positions of the particles were identical in order to check the accuracy of the UNIT network. For the reduction prediction of the real structure, segmented SEM images were used as training and validation data. Raw SEM images of NiO-YSZ and Ni-YSZ anodes are shown in Supplementary Figs. 3–5 in the supplementary materials. Only the homogonous regions of functional layers were used for training, and the size of training images was 700–1300 µm². The validation using real microstructures is challenging, as it is not possible from SEM to obtain an identical sample pair before and after reduction. Therefore, statistical parameters are compared between real and artificially reduced samples. Two types of input data were used for NiO-YSZ electrodes, i.e. images used for training and different microstructure taken from the same sample. In the case of NiO-GDC electrodes, two samples were used for training and another sample is used for validation. For time-dependent NiO-YSZ reduction, only one initial microstructural image was available.

Table 2 | Discriminators architecture

Type	PatchGAN discriminator
Input size	$64 \times 64 \times 3$ or $256 \times 256 \times 3$
Number of down sampling blocks	4
Filter size	3
Weight initialization used in convolution layers	Normal distribution with zero mean and standard deviation 0.01
Normalization layer	None
Padding	Pad with 0
Activation function	Leaky Rectified Linear Unit with 0.2 scale factor
Activation function after final convolution	None

Table 3 | Number and size of training images for toy problems

Training model		Number of training images	Size of training images, pixel × pixel	Number of validation images	Size of validation images, pixel × pixel
Toy problem 1 (single particle)	Sintered	100	64×64	200	64×64
	Reduced	100	64×64	200	64×64
Toy problem 1 (multiple particles)	Sintered	100	64×64	200	64×64
	Reduced	100	64×64	200	64×64
Toy problem 2	Sintered	20	256×256	200	256×256
	Reduced	20	256×256	200	256×256
Toy problem 3	Sintered	5	256×256	64	256×256
	Reduced	5	256×256	64	256×256

Adaptive moment estimation optimizer (Adam) was used for training using GPUs (NVIDIA A100), whose details are given in Table 5. Single training epoch took 1.2 s, where the networks were trained for 1000 – 5000 epochs.

Table 4 | Number and size of training images for reduction of Ni-based anodes

Training model		Number of images	Size of images	
			pixel × pixel	µm × µm
Ni-YSZ reduction	Sintered	3	524 × 956	19.6 × 35.8
			512 × 744 *	19.2 × 27.9 *
			512 × 726 *	19.2 × 27.2 *
	Reduced	1	524 × 956	19.6 × 35.8
Ni-GDC reduction	Sintered	3	Ni50GDC50: 488 × 1431	18.3 × 53.6
			Ni60GDC40-IP: 650 × 1433	24.3 × 53.7
			Ni60GDC40: 497 × 1431 *	18.6 × 53.6 *
	Reduced	3	Ni50GDC50: 556 × 952	20.8 × 35.7
			Ni60GDC40-IP: 544 × 936	20.4 × 35.1
			Ni60GDC40: 588 × 928 *	22.0 × 34.8 *
Ni-YSZ reduced at various temperatures	Sintered	3	524 × 956	19.6 × 35.8
			512 × 744 *	19.2 × 27.9 *
			512 × 726 *	19.2 × 27.2 *
	Reduced	4	500 °C: 544 × 1280	20.4 × 47.9
			600 °C: 592 × 1280	22.2 × 47.9
			800 °C: 524 × 956	19.6 × 35.8
			1000 °C: 539 × 1280	20.2 × 47.9
Ni-YSZ time dependent reduction	Sintered	1	672 × 952	25.2 × 35.7
	Reduced	4	5 s: 800 × 952	30.0 × 35.7
			15 s: 816 × 952	30.6 × 35.7
			30 s: 944 × 944	35.4 × 35.4
			1 h: 920 × 960	34.5 × 36.0

*Test data.

Utilizing the trained network for processing a new microstructure took 0.5 s for a single image. After training, the generator can process larger size of microstructures than the patch size incorporated in the training process. The trained UNIT generator can artificially produce reduced Ni structures from any new sintered sample image. The source-to-target translation path for the artificial reduction is represented by the red arrows in Fig. 9a.

Reduction experiment

Microstructure evolutions in the reduction process were investigated using two SOFC anode cermets as shown in Fig. 11. The electrolyte supported SOFCs with Ni-YSZ (Kusaka, Japan)[77] and Ni-GDC (AGC Seimi, Japan and ShinEtsu, Japan)[78] fuel electrodes were fabricated by screen-printing slurries on commercial YSZ pellets (Tosoh, Japan). The Ni-GDC electrode composition was controlled by mixing the powders at ratios of Ni : GDC = 50 : 50 vol.% (Ni50GDC50) and Ni : GDC = 60 : 40 vol.% (Ni60GDC40). Another sample Ni60GDC40-IP with a composition of Ni : GDC = 60 : 40 vol.% was prepared by isostatically pressing dried electrode green body at 200 MPa for 30 min to reduce porosity[78]. Pure NiO current collection layer was screen-printed on the top of the fuel electrodes. Anodes and current collector layers were sintered in air at 1350 °C for 3 h. The counter electrode was fabricated with GDC barrier layer and LSCF (Fuel Cell Materials, USA) cathode on the other side of the electrolyte. The anode active area was 0.785 cm^2 and the thickness of the NiO-YSZ (Ni-GDC) electrode and NiO current collector layer were approximately 18-20 and 5 µm, respectively.

The electrodes were reduced with two steps in the SOFC testing rig (Bel-SOFC, MicrotracBel, Japan). Firstly, 50 sccm of H$_2$: N$_2$ = 5 : 95% gas mixture was supplied for 30 min, and then pure hydrogen was provided. The time of pure hydrogen exposure was adjusted to 6, 4, 0.5, 0.5 h depending on the reduction temperatures conducted at 500, 600, 800, and 1000 °C, respectively. The open circuit voltage was monitored to ensure complete NiO reduction. Additionally, full reduction of NiO was confirmed by conducting EDX measurement.

An additional experiment was conducted to investigate the influence of reduction time for a given temperature. The cell was operated for 20 h prior to the oxidation-reduction experiment at 800 °C. Then, the anode was oxidized by supplying pure oxygen, flushed with nitrogen, and finally exposed to pure hydrogen. The hydrogen reduction time was set as 5 s, 15 s,

Table 5 | Details of the training procedure

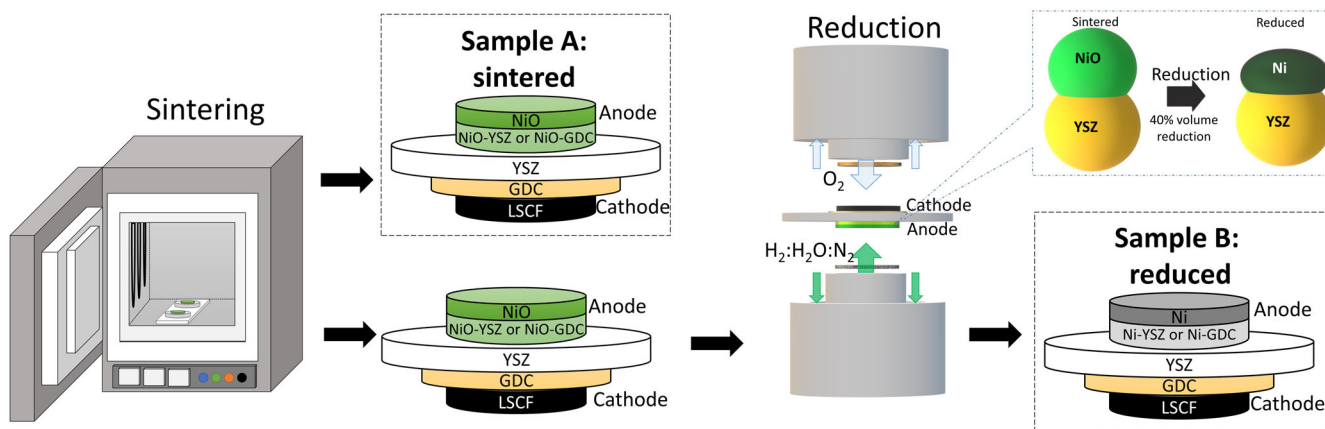| Optimizer	Adaptive moment estimation optimizer (Adam)
Learning rate	0.001
Gradient decay factor	0.5
Squared gradient decay factor	0.999

Fig. 11 | Experimental workflow.

30 s, 20 mins and 1 h. The samples were quenched to room temperature with supplying nitrogen. More details can be found in our previous work[73].

As-sintered and as-reduced samples were embedded in epoxy resin (Epofix, Struers), polished (Cross section polisher, JEOL, SM-09020CP), and observed with the scanning electron microscope (SEM, JSM-7001F, JEOL). The cross-sectional images were segmented by patch convolutional neural network in the encode-decoder configuration[54,79]. The microstructure parameters were calculated from the 2D cross-sections by Tau-Factor Matlab library[80]. The 3D value of TPB density was estimated from 2D images by the stereological formula as described in ref. [81].

Data availability
The datasets analyzed during the current study are available from the corresponding author on reasonable request.

Code availability
The underlying code for this study and training datasets may be made available to qualified researchers on reasonable request from the corresponding author.

References
1. Holzer, L. et al. Quantitative relationships between composition, particle size, triple phase boundary length and surface area in nickel-cermet anodes for Solid Oxide Fuel Cells. *J. Power Sources* **196**, 7076–7089 (2011).
2. Mogensen, M. B. et al. Ni migration in solid oxide cell electrodes: Review and revised hypothesis. *Fuel Cells* **21**, 415–429 (2021).
3. Fouquet, D., Müller, A. C., Weber, A. & Ivers-Tiffée, E. Kinetics of oxidation and reduction of Ni/YSZ cermets. *Ion. (Kiel.)* **9**, 103–108 (2003).
4. Shimura, T., Jiao, Z., Hara, S. & Shikazono, N. Quantitative analysis of solid oxide fuel cell anode microstructure change during redox cycles. *J. Power Sources* **267**, 58–68 (2014).
5. Sciazko, A., Komatsu, Y., Yokoi, R., Shimura, T. & Shikazono, N. Effects of mass fraction of $La_{0.9}Sr_{0.1}Cr_{0.5}Mn_{0.5}O_{3-\delta}$ and $Gd_{0.1}Ce_{0.9}O_{2-\delta}$ composite anodes for nickel free solid oxide fuel cells. *J. Eur. Ceram. Soc.* **42**, 1556–1567 (2022).
6. Zekri, A., Herbrig, K., Knipper, M., Parisi, J. & Plaggenborg, T. Nickel depletion and agglomeration in SOFC anodes during long-term operation. *Fuel Cells* **17**, 359–366 (2017).
7. Yu, F. et al. New insights into carbon deposition mechanism of nickel/yttrium-stabilized zirconia cermet from methane by in situ investigation. *Appl. Energy* **256**, 113910 (2019).
8. Jeangros, Q., Aebersold, A. B., Hébert, C., van herle, J. & Hessler-Wyser, A. A TEM study of Ni interfaces formed during activation of SOFC anodes in H2: Influence of grain boundary symmetry and segregation of impurities. *Acta Mater.* **103**, 442–447 (2016).
9. Liu, Y. L. & Jiao, C. Microstructure degradation of an anode/electrolyte interface in SOFC studied by transmission electron microscopy. *Solid State Ion.* **176**, 435–442 (2005).
10. Matsuzaki, Y. The poisoning effect of sulfur-containing impurity gas on a SOFC anode: Part I. Dependence on temperature, time, and impurity concentration. *Solid State Ion.* **132**, 261–269 (2000).
11. Harris, W. M. et al. Three-dimensional microstructural imaging of sulfur poisoning-induced degradation in a Ni-YSZ anode of solid oxide fuel cells. *Sci. Rep.* **4**, 1–7 (2014).
12. Wang, Y. et al. Ni migration of Ni-YSZ electrode in solid oxide electrolysis cell: An integrated model study. *J. Power Sources* **516**, 230660 (2021).
13. Xiang, Y., Da, Y., Shikazono, N. & Jiao, Z. Quantitative study on solid oxide fuel cell anode microstructure stability based on 3D microstructure reconstructions. *J. Power Sources* **477**, 228653 (2020).
14. Jiao, Z. & Shikazono, N. Simulation of the reduction process of solid oxide fuel cell composite anode based on phase field method. *J. Power Sources* **305**, 10–16 (2016).
15. Hara, S., Ohi, A. & Shikazono, N. Sintering analysis of sub-micron-sized nickel powders: Kinetic Monte Carlo simulation verified by FIB-SEM reconstruction. *J. Power Sources* **276**, 105–112 (2015).
16. Ge, X. M., Chan, S. H., Liu, Q. L. & Sun, Q. Solid oxide fuel cell anode materials for direct hydrocarbon utilization. *Adv. Energy Mater.* **2**, 1156–1181 (2012).
17. Jiao, Z. & Shikazono, N. Study on the effects of polarization on local morphological change of nickel at active three-phase-boundary using patterned nickel-film electrode in solid oxide fuel cell anode. *Acta Mater.* **135**, 124–131 (2017).
18. Gil, V., Larrea, A., Merino, R. I. & Orera, V. M. Redox behaviour of Gd-doped ceria–nickel oxide composites. *J. Power Sources* **192**, 180–184 (2009).
19. Kishimoto, H. et al. Agglomeration behavior of nickel particles on YSZ electrolyte. *Solid State Ion.* **225**, 65–68 (2012).
20. Kishimoto, M., Iwai, H., Saito, M. & Yoshida, H. Quantitative evaluation of solid oxide fuel cell porous anode microstructure based on focused ion beam and scanning electron microscope technique and prediction of anode overpotentials. *J. Power Sources* **196**, 4555–4563 (2011).
21. Ouyang, M. et al. Model-guided design of a high performance and durability Ni nanofiber/ceria matrix solid oxide fuel cell electrode. *J. Energy Chem.* **56**, 98–112 (2021).
22. Shu, L. et al. Advanced perovskite anodes for solid oxide fuel cells: A review. *Int J. Hydrog. Energy* **44**, 31275–31304 (2019).
23. Park, B. H. & Choi, G. M. Ex-solution of Ni nanoparticles in a $La_{0.2}Sr_{0.8}Ti_{1-x}Ni_xO_{3-\delta}$ alternative anode for solid oxide fuel cell. *Solid State Ion.* **262**, 345–348 (2014).
24. Wankmüller, F. et al. Multi-scale characterization of ceramic inert-substrate-supported and co-sintered solid oxide fuel cells. *J. Mater. Sci.* **55**, 11120–11136 (2020).
25. Jouttijärvi, S., Asghar, M. I. & Lund, P. D. Microscopic techniques for analysis of ceramic fuel cells. *Wiley Interdiscip. Rev. Energy Environ.* **7**, e299 (2018).
26. de Angelis, S. et al. Tracking nickel oxide reduction in solid oxide cells via ex-situ ptychographic nano-tomography. *Mater. Charact.* **162**, 110183 (2020).
27. Chen-Wiegart, Y. K., Kennouche, D., Scott Cronin, J., Barnett, S. A. & Wang, J. Effect of Ni content on the morphological evolution of Ni-YSZ solid oxide fuel cell electrodes. *Appl. Phys. Lett.* **108**, 083903 (2016).
28. Ouyang, Z. et al. Operando observations of active three phase boundary of patterned nickel - Yttria stabilized zirconia electrode in solid oxide cell. *J. Power Sources* **529**, 231228 (2022).
29. Komatsu, Y. et al. Operando observation of patterned nickel - gadolinium doped ceria solid oxide fuel cell anode. *J. Power Sources* **516**, 230670 (2021).
30. Jeangros, Q. et al. Benefits of nanoscale operando experiments in environmental transmission electron microscopy for solid oxide fuel cell devices. *Microsc. Microanalysis* **28**, 814–816 (2022).
31. Sciazko, A., Komatsu, Y. & Shikazono, N. Unsupervised generative adversarial network for 3-D microstructure synthesis from 2-D image. *ECS Trans.* **103**, 1363–1373 (2021).
32. Saito, Y. et al. Deep-learning-based quality filtering of mechanically exfoliated 2D crystals. *NPJ Comput. Mater.* **5**, 1–6 (2019).
33. Gayon-Lombardo, A., Mosser, L., Brandon, N. P. & Cooper, S. J. Pores for thought: generative adversarial networks for stochastic reconstruction of 3D multi-phase electrode microstructures with periodic boundaries. *NPJ Comput. Mater.* **6**, 1–11 (2020).
34. Wu, H., Fang, W. Z., Kang, Q., Tao, W. Q. & Qiao, R. Predicting effective diffusivity of porous media from images by deep learning. *Sci. Rep.* **9**, 1–12 (2019).

35. Liu, M. Y., Breuel, T. & Kautz, J. Unsupervised image-to-image translation networks. *Adv. Neural Inf. Process Syst.* **2017**, 701–709 (2017).

36. Wang, W. et al. Resolution enhancement in microscopic imaging based on generative adversarial network with unpaired data. *Opt. Commun.* **503**, 127454 (2022).

37. Zhang, C. et al. Correction of out-of-focus microscopic images by deep learning. *Comput. Struct. Biotechnol. J.* **20**, 1957–1966 (2022).

38. Li, X. et al. Unsupervised content-preserving transformation for optical microscopy. *Light Sci. Appl.* **10**, 44 (2021).

39. Ming, W. et al. A systematic review of machine learning methods applied to fuel cells in performance evaluation, durability prediction, and application monitoring. *Int. J. Hydrog. Energy* **48**, 5197–5228 (2023).

40. Brus, G. Overcoming a recent impasse in the application of artificial neural networks as solid oxide fuel cells simulator with computational topology. *Energy AI* **14**, 100291 (2023).

41. Zhai, S. et al. A combined ionic Lewis acid descriptor and machine-learning approach to prediction of efficient oxygen reduction electrodes for ceramic fuel cells. *Nat. Energy* **7**, 866–875 (2022).

42. Subotić, V., Eibl, M. & Hochenauer, C. Artificial intelligence for time-efficient prediction and optimization of solid oxide fuel cell performances. *Energy Convers. Manag.* **230**, 113764 (2021).

43. Arriagada, J., Olausson, P. & Selimovic, A. Artificial neural network simulator for SOFC performance prediction. *J. Power Sources* **112**, 54–60 (2002).

44. Mütter, F. et al. Artificial intelligence for solid oxide fuel cells: Combining automated high accuracy artificial neural network model generation and genetic algorithm for time-efficient performance prediction and optimization. *Energy Convers. Manag.* **291**, 117263 (2023).

45. Xia, L., Khosravi, A., Han, M. & Sun, L. Artificial intelligence based structural optimization of solid oxide fuel cell with three-dimensional reticulated trapezoidal flow field. *Int. J. Hydrog. Energy* **48**, 28131–28149 (2023).

46. Buchaniec, S., Sciazko, A., Mozdzierz, M. & Brus, G. A novel approach to the optimization of a solid oxide fuel cell anode using evolutionary algorithms. *IEEE Access.* **7**, 34361–34372 (2019).

47. Le, G. T., Mastropasqua, L., Brouwer, J. & Adler, S. B. Simulation-informed machine learning diagnostics of solid oxide fuel cell stack with electrochemical impedance spectroscopy. *J. Electrochem. Soc.* **169**, 034530 (2022).

48. Tanveer, W. H. et al. Improving fuel cell performance via optimal parameters identification through fuzzy logic based-modeling and optimization. *Energy* **204**, 117976 (2020).

49. Xu, H. et al. Towards online optimisation of solid oxide fuel cell performance: Combining deep learning with multi-physics simulation. *Energy AI* **1**, 100003 (2020).

50. Yan, Z., He, A., Hara, S. & Shikazono, N. Modeling of solid oxide fuel cell (SOFC) electrodes from fabrication to operation: Correlations between microstructures and electrochemical performances. *Energy Convers. Manag.* **190**, 1–13 (2019).

51. Peng, J. et al. Generalized spatial-temporal fault location method for solid oxide fuel cells using LSTM and causal inference. *IEEE Trans. Transp. Electr.* **8**, 4583–4594 (2022).

52. Sheng, C. et al. A comparative study of the Kalman filter and the lstm network for the remaining useful life prediction of SOFC. *Energies* **16**, 3628 (2023).

53. Lyu, Z. et al. Prediction of fuel cell performance degradation using a combined approach of machine learning and impedance spectroscopy. *J. Energy Chem.* **87**, 32–41 (2023).

54. Sciazko, A., Komatsu, Y., Shimura, T. & Shikazono, N. Segmentation of solid oxide cell electrodes by patch convolutional neural network. *J. Electrochem. Soc.* **168**, 044504 (2021).

55. Hwang, H. et al. Integrated application of semantic segmentation-assisted deep learning to quantitative multi-phased microstructural analysis in composite materials: Case study of cathode composite materials of solid oxide fuel cells. *J. Power Sources* **471**, 228458 (2020).

56. Wang, Y. et al. Phase segmentation of Ni/YSZ anode for solid oxide fuel cells by deep learning. *ECS Trans.* **111**, 457–467 (2023).

57. Yamagishi, R. et al. Super-resolved in-operando observation of SOFC pattern electrodes. *ECS Trans.* **103**, 2087–2098 (2021).

58. Sciazko, A., Komatsu, Y., Shimura, T. & Shikazono, N. Electrode microstructure reconstruction from FIB-SEM datasets with anisotropic resolutions. *Proc. JSME Natl. Symp. Power Energy Syst.* **2021**, C212 (2021).

59. Wang, H., Yin, Y., Hui, X. Y., Bai, J. Q. & Qu, Z. G. Prediction of effective diffusivity of porous media using deep learning method based on sample structure information self-amplification. *Energy AI* **2**, 100035 (2020).

60. Kondo, R., Yamakawa, S., Masuoka, Y., Tajima, S. & Asahi, R. Microstructure recognition using convolutional neural networks for prediction of ionic conductivity in ceramics. *Acta Mater.* **141**, 29–38 (2017).

61. Yang, Z. et al. Establishing structure-property localization linkages for elastic deformation of three-dimensional high contrast composites using deep learning approaches. *Acta Mater.* **166**, 335–345 (2019).

62. Ding, Z., Pascal, E. & De Graef, M. Indexing of electron back-scatter diffraction patterns using a convolutional neural network. *Acta Mater.* **199**, 370–382 (2020).

63. Liu, X. et al. Correlation between microstructures and macroscopic properties of nickel/yttria-stabilized zirconia (Ni-YSZ) anodes: Meso-scale modeling and deep learning with convolutional neural networks. *Energy AI* **7**, 100122 (2022).

64. Liu, X., Yan, Z. & Zhong, Z. Predicting elastic modulus of porous La0.6Sr0.4Co0.2Fe0.8O3-δ cathodes from microstructures via FEM and deep learning. *Int. J. Hydrog. Energy* **46**, 22079–22091 (2021).

65. Hsu, T. et al. Microstructure generation via generative adversarial network for heterogeneous, topologically complex 3D materials. *JOM* **73**, 90–102 (2021).

66. Kishimoto, M., Matsui, Y. & Iwai, H. Conditional generative adversarial network for generation of three-dimensional porous structure of solid oxide fuel cell anodes with controlled volume fractions. *J. Power Sources* **580**, 233411 (2023).

67. Zhou, S. et al. Real-time data-driven fault diagnosis of proton exchange membrane fuel cell system based on binary encoding convolutional neural network. *Int. J. Hydrog. Energy* **47**, 10976–10989 (2022).

68. Shri Prakash, B., Senthil Kumar, S. & Aruna, S. T. Properties and development of Ni/YSZ as an anode material in solid oxide fuel cell: A review. *Renew. Sustain. Energy Rev.* **36**, 149–179 (2014).

69. Jørgensen, P. S., Ebbehøj, S. L. & Hauch, A. Triple phase boundary specific pathway analysis for quantitative characterization of solid oxide cell electrode microstructure. *J. Power Sources* **279**, 686–693 (2015).

70. Jiao, Z. & Shikazono, N. Quantitative study on the correlation between solid oxide fuel cell Ni-YSZ composite anode performance and reduction temperature based on three-dimensional reconstruction. *J. Electrochem. Soc.* **162**, F571–F578 (2015).

71. Andrzejczuk, M. et al. Microstructural changes in NiO–ScSZ composite following reduction processes in pure and diluted hydrogen. *Mater. Charact.* **87**, 159–165 (2014).

72. Jeangros, Q. et al. In situ redox cycle of a nickel-YSZ fuel cell anode in an environmental transmission electron microscope. *Acta Mater.* **58**, 4578–4589 (2010).

73. Shimura, T., Jiao, Z., Hara, S. & Shikazono, N. Investigation of microstructural change of nickel-yttria stabilized zirconia anode

during oxidation and reduction based on three-dimensional reconstruction. *J. Electrochem. Soc.* **164**, F147–F153 (2017).

74. Han, Z., Dong, H., Yang, Y. & Yang, Z. Achieving robust redox stability of SOFC through Ni-YSZ anode layer thinning and inert support mechanical compensation. *ACS Appl. Energy Mater*. https://doi.org/10.1021/acsaem.2c00182 (2022).

75. Manukyan, K. V. et al. Nickel oxide reduction by hydrogen: kinetics and structural transformations. *J. Phys. Chem. C.* **119**, 16131–16138 (2015).

76. Karniadakis, G. E. et al. Physics-informed machine learning. *Nat. Rev. Phys.* **3**, 422–440 (2021).

77. Sciazko, A., Shimura, T., Komatsu, Y. & Shikazono, N. Ni-GDC and Ni-YSZ electrodes operated in solid oxide electrolysis and fuel cell modes. *J. Therm. Sci. Technol.* **16**, JTST0013–JTST0013 (2021).

78. Komatsu, Y., Sciazko, A. & Shikazono, N. Isostatic pressing of screen printed nickel-gadolinium doped ceria anodes on electrolyte-supported solid oxide fuel cells. *J. Power Sources* **485**, 229317 (2021).

79. Miyahara, K., Sciazko, A., Shimura, T., Jiao, Z. & Shikazono, N. Evaluation of the influence of gadolinium doped ceria particle size on the electrochemical performance and microstructure of nickel-gadolinium doped ceria anodes. *ECS Trans.* **78**, 1149–1159 (2017).

80. Cooper, S. J., Bertei, A., Shearing, P. R., Kilner, J. A. & Brandon, N. P. TauFactor: An open-source application for calculating tortuosity factors from tomographic data. *Softw.X* **5**, 203–210 (2016).

81. Shikazono, N., Sakamoto, Y., Yamaguchi, Y. & Kasagi, N. Microstructure and polarization characteristics of anode supported tubular solid oxide fuel cell with co-precipitated and mechanically mixed Ni-YSZ anodes. *J. Power Sources* **193**, 530–540 (2009).

Acknowledgements

Author contributions

AS, YK and NS conceptualized research idea and designed research framework. AS, YK and TS conducted experimental research on SOFC reduction; AS and YK prepared numerical codes and conducted machine learning experiments. AS, YK and NS co-wrote and revised manuscript. All authors discussed the results and approved the final version of the paper.

Competing interests

The authors declare no competing interests.

Additional information

Supplementary information The online version contains supplementary material available at https://doi.org/10.1038/s41524-024-01228-3.

Correspondence and requests for materials should be addressed to Anna Sciazko.

Reprints and permissions information is available at http://www.nature.com/reprints

Publisher's note Springer Nature remains neutral with regard to jurisdictional claims in published maps and institutional affiliations.